Terahertz MIMO Fading Analysis and Doppler Modeling in a Data Center Environment

Chia-Lin Cheng, Seun Sangodoyin, and Alenka Zajić
Georgia Institute of Technology, Atlanta, GA 30332 USA

***Abstract*— In this paper, we present results from a Terahertz (THz) channel measurement campaign in a data center environment. We analyze propagation parameters, such as pathloss, shadowing gain, and RMS delay spread. Amplitude fading statistics in a 4×4 Multiple-Input-Multiple-Output (MIMO) channel are also investigated. Furthermore, Doppler shift in THz bands due to the effect of cooling airflow turbulence, which causes cables (lying in the wireless propagation path) to vibrate is also measured. A two-dimensional (2-D) geometrical propagation model that includes moving scatterers (cables) is introduced. From the 2-D model, a corresponding Doppler power spectrum (DPS) is derived and validated with measured data. This work is pertinent to THz wireless systems design for a data center environment.**

***Index Terms*— Wireless data centers, THz communications, MIMO, channel measurements, channel modeling, statistical channel model, Doppler power spectrum.**

I. Introduction

Cloud computing for on-demand computing services, such as storage and data processing, has become popular in recent years. Increasing demand for cloud computing is driving the need for data centers with low-latency network and capability for dynamic reconfiguration based on workload [1].

In traditional data centers, information exchange between servers mainly relies on metal wires and optical fiber cables. The use of the wires and cables increases the service time and the cost of assembly, operation, and maintenance. Wired typologies impact the flexibility and scalability of the overall data center. Furthermore, cable bundles between racks can cause blockages of airflow and lead to inefficient cooling. Recent literatures introduce additional Terahertz (THz) wireless links in data centers for the purpose of achieving higher reconfigurability and dynamic operation [1]–[3]. In addition, THz frequencies promise a higher data rate with its available bandwidth and lower interference due to the directional antennas.

The development of THz wireless systems in data centers requires the characterization of the propagation channel in which the device will operate. Stochastic channel model and simulation results for THz wireless data centers are presented in [4], [5]. However, there were no measurement-based results provided. A THz measurement campaign in a data center was presented in [6], showing that path attenuation is comparable to Friis theoretical values and that THz wireless communication in a data center is possible. However, the measurement campaign did not investigate the scenario with obstruction of cables, which are common objects in data centers. In our previous work [7]–[9], THz channel sounding has been conducted in a data center-like environment for the study of various potential THz communication scenarios in a data center. The impacts of obstructions of cables, server racks and their mesh structures on THz propagation were investigated, and the corresponding channel properties were developed. Moreover, a blade-to-blade (B2B) link for the communication between vertically stacked servers has been proposed. However, these prior measurements were not conducted in an actual data center but a mockup model of data center.

In this paper, we investigate the amplitude fading statistics of MIMO channel in a data center environment. Furthermore, Doppler shift in THz bands due to the effect of cooling airflow turbulence, which causes loosely bundled cables to vibrate is also measured. We then introduce a two-dimensional (2-D) geometrical propagation model that includes moving scatterers. From the 2-D model, the corresponding Doppler power spectrum (DPS) is derived and compared with measured data. Note that the loosely bundled cables referred to in this work comprises of power and auxiliary cables.

The rest of the paper is organized as follows. The THz measurement setup is introduced in Section II. Section III introduces the analysis methodology and results. Finally, concluding remarks are presented in Section IV.

II. Measurement Campaign

The measurement campaign was conducted in a data center at the Tech Way Building on the campus of the Georgia Institute of Technology, Atlanta, GA. Frequency-domain channel sounding was performed with a Keysight N5224A PNA vector network analyzer (VNA) and Virginia Diodes, Inc. (VDI) transceivers (Tx210/Rx148) [10] over a bandwidth of 12 GHz (300–312 GHz) with 801 frequency tones. A -15 dBm output power was transmitted. A vertically polarized pyramidal horn antenna with gain that varies from 22 to 24 dBi from 300 to 320 GHz was used for this experiment. The nominal half-power beamwidth (HPBW) of the horn antenna is about 10° in azimuth and elevation.

We investigate an obstructed-line-of-sight (OLoS) scenario where the wireless channel is obstructed by objects commonly found in data centers such as the aforementioned power and auxiliary cables. The two OLoS scenarios investigated are subsequently discussed.

*1) **OLoS Link With Stationary Cables Serving as Obstruction**:* THz signals are suitable for short-range point-to-point

This work has been supported, in part, by NSF grant 1651273. The views and findings in this paper are those of the authors and do not necessarily reflect the views of NSF.

communication [3], which can be established between adjacent server racks in a data center as shown in Fig. 1. In such cases, cluster of power cables could serve as obstruction blocking the line-of-sight (LoS) link between the Transmitter (Tx) and Receiver (Rx). The surrounding environment mostly consists of metal structures of the server racks. Towards diversity reasons, we conduct measurements using a 4×4 *virtual* MIMO uniform linear array (ULA) configuration [8] with 1 mm step size between antenna array elements to achieve 16 channel realizations at Tx-Rx separation, d = 15 cm as illustrated in Fig. 2 (a).

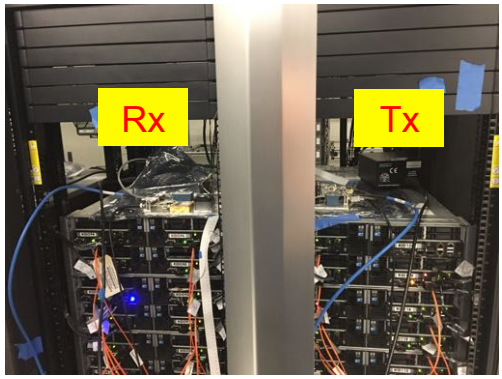

Fig. 1. Measurement setup for the OLoS link with stationary cables serving as obstruction.

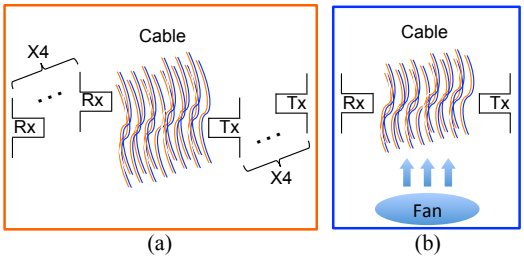

Fig. 2. Illustrations of (a) the 4×4 MIMO ULA configuration for the OLoS link with obstruction of stationary cables and (b) the OLoS link with vibrating cables serving as obstruction.

*2) **OLoS Link With Vibrating Cables Serving as Obstruction**:* The existence of loosely bundled cables in data centers between server racks and compartments [11] could have impacts on rack-to-rack communication. This is an especially important case where the turbulence from cooling airflow in the data center can cause the cable to vibrate, and thus lead to Doppler shift in the THz bands. To characterize the aforementioned Doppler shift in this type of data center scenario, we consider a fixed wireless scenario in which the Tx and Rx were stationary with the cable(s) serving as the moving scatterer [12]–[15]. It is important to note that for this experiment, a slightly different measurement setup was assembled such that a separate narrow-band measurement was performed in an indoor lab environment following a similar arrangement in Fig. 1. Our setup is illustrated in Fig. 2 (b), where a cooling fan was placed underneath the cable cluster to create the turbulence, and Tx-Rx distance is 40 cm. The fan was placed 30 cm below the Tx/Rx to ensure its enclosure did not interfere with the propagation channel.

III. Analysis Methodology and Results

In this section, we analyze the measured pathloss, shadowing gain (X_σ), RMS delay spread (τ_{rms}), and amplitude fading statistics of a 4×4 MIMO channel. The modeling procedure for the Doppler power spectrum is also presented.

A. Pathloss, Shadowing Gain, and Delay Spread

In this section, we characterize the measured pathloss, shadowing gain, and τ_{rms} in a 4×4 MIMO channel with stationary cables serving as obstruction as introduced in Figs. 1 and 2 (a). The mean of measured pathloss ($\overline{PL}$) is calculated by averaging a complete frequency response over frequency and time,

$$\overline{PL(d)} = \frac{1}{MN}\sum_{i=1}^{N}\sum_{j=1}^{M}|H(f_i,t_j,d)|^2, \tag{1}$$

where M is the number of snapshots of frequency-response over time, N is the number of frequency tones. $H(f_i,t_j,d)$ is the measured complex frequency response data (transfer function) and d is the Tx-Rx distance. Cumulative distribution functions (CDFs) of the shadowing gain (X_σ) and τ_{rms} are presented in Figs. 3 (a) and (b), respectively. The mean (μ) of measured pathloss is found to be 87.75 dB and the standard deviation (σ) of its shadowing gain is 6.03 dB. The τ_{rms} has μ = -94.13 dB and σ = 2.31 dB.

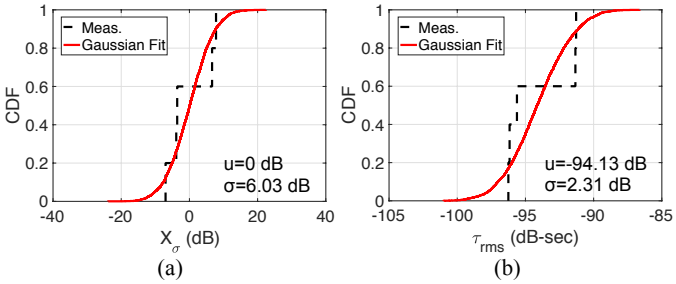

Fig. 3. CDFs of the (a) shadowing gain (X_σ) and (b) τ_{rms} in the 4×4 MIMO channel with cables as obstruction.

B. Amplitude Fading Statistics

In this section, we characterize the signal's amplitude fading statistics caused by the cable clusters in a 4×4 MIMO channel with stationary cables serving as obstruction as introduced in Figs. 1 and 2 (a). We have found that the distribution of the signal amplitude fading can be modeled by m-Nakagami distribution, where the m-parameter in dB can be modeled as a truncated Gaussian distribution denoted by m– $(T_N(\mu_m(dB),\sigma_m^2(dB))$ with a CDF shown in Fig. 4. The mean (μ_m) and standard deviation (σ_m) of the m-parameter have also been modeled as a function of the delay bin (τ_k) of the PDP at each shadowing point, which can be expressed as,

$$\mu_m(\tau_k) = A - \frac{1}{B}\tau_k, \tag{2}$$

$$\sigma_m(\tau_k) = C - \frac{1}{D}\tau_k, \tag{3}$$

where the unit of τ_k is in nanosecond. Linear fit results are shown in Fig. 5, and the corresponding values of slope and intercept are stated in Table I.

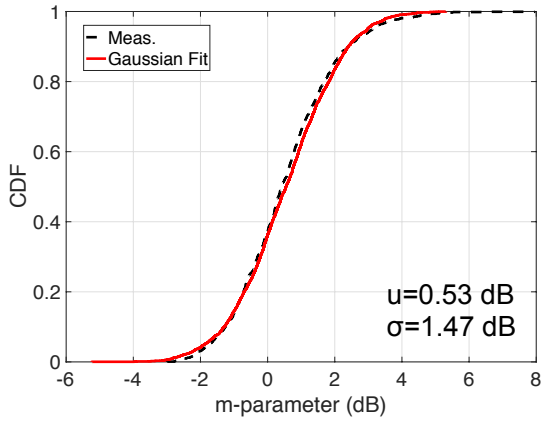

Fig. 4. CDF of the m-parameter (dB) using an ensemble of shadowing points.

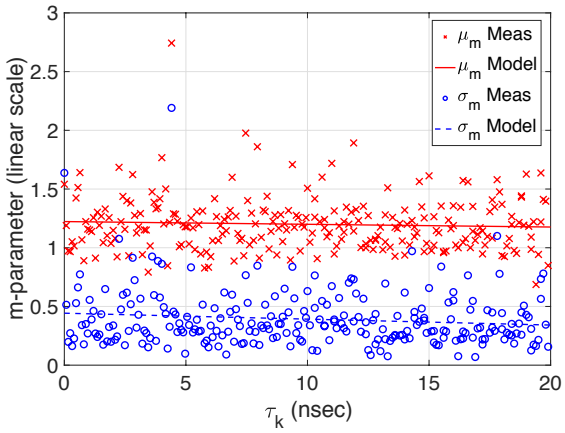

Fig. 5. Linear model for the mean (μ_m) and standard deviation (σ_m) of the m-parameter as a function of delay bin (τ_k).

C. Modeling of Doppler Power Spectrum

In this section, we investigate a scenario where vibration of cables caused by turbulence from the cooling airflow can lead to Doppler shift in the THz bands as shown in Fig. 2 (b). A 2-D narrow-band geometrical model that is modified from [15] is introduced to model the corresponding Doppler power spectrum. The Doppler shift (or "spread") is important in determining the minimum signalling rate allowable for coherent demodulation and the minimum adaption rate for an adaptive receiver [12].

In Fig. 6, the two-ring model defines two rings separated by distance D, one around the Tx ($A_T^{(p)}$) with radius of R_T and the other around the Rx ($A_R^{(q)}$) with radius of R_R, along with the line-of-sight (LoS) ray, single-bounced ray at the transmit side (SBT), and single-bounced ray at the receive side (SBR). Two moving scatterers, $S_{TM}^{(k)}$, and $S_{RM}^{(l)}$, lie on the rings centered at the Tx and Rx, respectively. Both Tx and Rx are stationary while $S_{TM}^{(k)}$ and $S_{RM}^{(l)}$ are moving with relative speeds v_{TS} and v_{RS} with respect to the Tx and Rx, respectively, in the directions described by angles $\gamma_{TS}^{(k)}$ and $\gamma_{RS}^{(l)}$ relative to the x-axis, respectively. θ_T and θ_R are the

TABLE I
SIGNAL AMPLITUDE STATISTICS

Scenario	A	B	C	D
4X4 MIMO	1.22	429.8	0.44	197.9

half power beamwidths of the Tx and Rx antennas relative to the x-axis, respectively. $\alpha_{TM}^{(k)}$ and $\alpha_{RM}^{(l)}$ are the angle of departure and the angle of arrival from moving scatterers, respectively. ϵ_{pk}, ϵ_{kq}, ϵ_{pl}, and ϵ_{lq} are the distances $A_T^{(p)}$–$S_{TM}^{(k)}$, $S_{TM}^{(k)}$–$A_R^{(q)}$, $A_T^{(p)}$–$S_{RM}^{(l)}$, and $S_{RM}^{(l)}$–$A_R^{(q)}$, respectively. For the ease of reference, the definitions of the parameters used in the model are summarized in the second column in Table II.

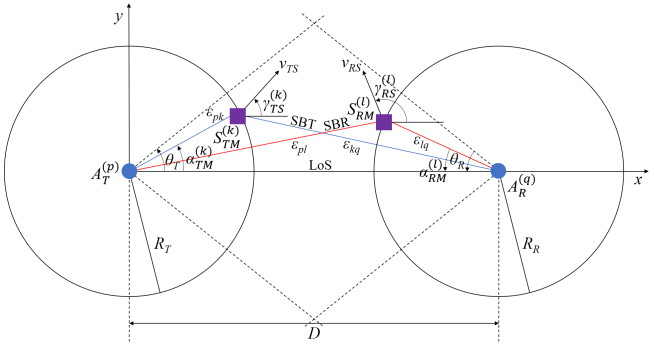

Fig. 6. The two-ring model with LoS, SBT, SBR rays and moving scatterers.

The complex impulse response of the $A_T^{(p)}$–$A_R^{(q)}$ link under narrow-band frequency-flat fading can be expressed as a superposition of LoS, SBT, and SBR rays,

$$h(t) = h^{\mathrm{LoS}}(t) + h^{\mathrm{SBT}}(t) + h^{\mathrm{SBR}}(t), \tag{4}$$

where corresponding components are

$$h^{\mathrm{LoS}}(t) = \sqrt{\Omega_{pq}}\sqrt{\frac{K}{K+1}}e^{\left(j2\pi f_{pq}^{\mathrm{LoS}}t - j\frac{2\pi}{\lambda}D\right)}, \tag{5}$$

$$h^{\mathrm{SBT}}(t) = \sqrt{\Omega_{pq}}\lim_{M_M\to\infty}\sum_{k=1}^{M_M}\sqrt{\frac{\eta_{TM}}{(K+1)}}\frac{1}{\sqrt{M_M}}\cdot e^{\left(j2\pi f_k^{\mathrm{SBT}}t - j\frac{2\pi}{\lambda}(\epsilon_{pk}+\epsilon_{kq}) + j\phi_{pq,k}^{\mathrm{SBT}}\right)}, \tag{6}$$

$$h^{\mathrm{SBR}}(t) = \sqrt{\Omega_{pq}}\lim_{N_M\to\infty}\sum_{k=1}^{N_M}\sqrt{\frac{\eta_{RM}}{(K+1)}}\frac{1}{\sqrt{N_M}}\cdot e^{\left(j2\pi f_l^{\mathrm{SBR}}t - j\frac{2\pi}{\lambda}(\epsilon_{pl}+\epsilon_{lq}) + j\phi_{pq,l}^{\mathrm{SBR}}\right)}, \tag{7}$$

where K is the Rice factor, $\Omega_{pq} = (D^{-\gamma/2}\sqrt{G_T G_R}\lambda/4\pi)^2$ is the power associated with the pq^{th} path, D is the Tx-Rx distance, γ is the pathloss exponent, G_T and G_R are the gains of the transmit and receive antennas, and λ is the wavelegnth, respectively. We assume the relative power allocated to the SBT and SBR is $\eta_{TM} + \eta_{RM} = 1$. M_M and N_M represent the number of the moving omnidirectional scatterers that lie on the Tx and Rx rings, respectively. f_{pq}^{LoS}, f_k^{SBT}, and f_l^{SBR} are the Doppler frequencies, where $f_{pq}^{\mathrm{LoS}} = 0$ given a fixed

wireless communication scenario with stationary Tx and Rx, while f_k^{SBT} and f_l^{SBR} can be simplified as [15]

$$f_k^{\mathrm{SBT}} = -f_{\mathrm{TSmax}}\left[\cos\left(\alpha_{TM}^{(k)} - \gamma_{TS}^{(k)}\right) - \cos\gamma_{TS}^{(k)}\right], \quad (8)$$

$$f_l^{\mathrm{SBR}} = -f_{\mathrm{RSmax}}\left[\cos\left(\alpha_{RM}^{(l)} - \gamma_{RS}^{(l)}\right) - \cos\gamma_{RS}^{(l)}\right], \quad (9)$$

where $f_{\mathrm{TSmax}} = v_{TS}/\lambda$ and $f_{\mathrm{RSmax}} = v_{RS}/\lambda$ are the maximum Doppler frequencies associated with the moving scatterers around the Tx and Rx, respectively. Note that when the number of scatterers at the Tx and Rx, i.e., M_M and N_M, approaches infinity, random variables of $\alpha_{TM}^{(k)}$, $\alpha_{RM}^{(l)}$, $\gamma_{TS}^{(k)}$, and $\gamma_{RS}^{(l)}$ can be characterized as continuous random variables with specified PDF. We use the von Mises PDF to characterize the aforementioned parameters since it approximates various common distributions (e.g., uniform, Gaussian, Laplacian) and gives closed-form solutions for many useful situations. The von Mises PDF is defined as $p(\theta) = \exp\left[\kappa\cos(\theta-\mu)\right]/2\pi I_0(\kappa)$ [16] where $\theta \in [-\pi, \pi)$, $I_0(\cdot)$ is the zeroth-order modified Bessel function of the first kind, $\mu \in [-\pi, \pi)$ is the mean angle where the scatterers are distributed in the x-y plane, and κ controls the spread of scatterers around the mean value. Phases $\phi_{pq,k}^{\mathrm{SBT}}$ and $\phi_{pq,l}^{\mathrm{SBR}}$ are assumed as independent random variables that are uniformly distributed on the interval $[0, 2\pi)$. Path lengths $\epsilon_{pk} = \epsilon_{lq} = \epsilon_{pl} = \epsilon_{kq} =$ 20 cm.

The autocorrelation function of the narrow-band complex channel impulse response in (4) is defined as,

$$R(\Delta t) = \frac{E\left[h(t)^* \cdot h(t+\Delta t)\right]}{\sqrt{Var\left[h(t)\right] Var\left[h(t)\right]}}, \quad (10)$$

where $(\cdot)^*$ is the complex conjugate operation, $E[\cdot]$ represents the statistical expectation operator, and $Var[\cdot]$ is the statistical variance operator. Since $h^{\mathrm{LoS}}(t)$, $h^{\mathrm{SBT}}(t)$, and $h^{\mathrm{SBR}}(t)$ are independent complex Gaussian random processes, (10) can be simplified to

$$R(\Delta t) = R^{\mathrm{LoS}}(\Delta t) + R^{\mathrm{SBT}}(\Delta t) + R^{\mathrm{SBR}}(\Delta t), \quad (11)$$

where $R^{\mathrm{LoS}}(\Delta t)$, $R^{\mathrm{SBT}}(\Delta t)$, $R^{\mathrm{SBR}}(\Delta t)$ are the autocorrelation functions of the LoS, SBT, and SBR components, respectively, and can be expressed as

$$R^{\mathrm{LoS}}(\Delta t) = \frac{K}{K+1} e^{-j\frac{4\pi}{\lambda}D}, \quad (12)$$

$$R^{\mathrm{SBT}}(\Delta t) = \frac{\eta_{TM}}{K+1} \cdot \int_0^{2\pi}\int_{-\theta_T}^{\theta_T} e^{j2\pi f_k^{\mathrm{SBT}}\Delta t} f(\alpha_{TM}) f(\gamma_{TS}) d\alpha_{TM} d\gamma_{TS}, \quad (13)$$

$$R^{\mathrm{SBR}}(\Delta t) = \frac{\eta_{RM}}{K+1} \cdot \int_0^{2\pi}\int_{-\theta_R}^{\theta_R} e^{j2\pi f_l^{\mathrm{SBR}}\Delta t} f(\alpha_{RM}) f(\gamma_{RS}) d\alpha_{RM} d\gamma_{RS}, \quad (14)$$

where $f(\alpha_{TM})$ and $f(\alpha_{RM})$ are characterized as uniform random variables distributed on the interval $[-7.5°, 7.5°]$, while $f(\gamma_{TS})$ and $f(\gamma_{RS})$ are characterized as von Mises PDFs, i.e., $f(\gamma_{TS}) = \exp\left[\kappa\cos(\gamma_{TS}-\mu)\right]/2\pi I_0(\kappa)$ and $f(\gamma_{RS}) = \exp\left[\kappa\cos(\gamma_{RS}-\mu)\right]/2\pi I_0(\kappa)$, respectively. The Doppler power spectrum of the narrow-band channel impulse response can then be estimated by calculating the Fourier transform of the autocorrelation function in (11), i.e.,

$$\begin{aligned} S(\nu) &= \mathcal{F}_{\Delta t}\{R(\Delta t)\} \\ &= \mathcal{F}_{\Delta t}\{R^{\mathrm{LoS}}(\Delta t) + R^{\mathrm{SBT}}(\Delta t) + R^{\mathrm{SBR}}(\Delta t)\}. \end{aligned} \quad (15)$$

TABLE II
DEFINITION OF THE PARAMETERS USED IN THE 2-D GEOMETRICAL MODEL

Parameters	Definition	Value
D	The distance between the centers of Tx and Rx sectors.	40 cm
R_T R_R	The radius of the Tx and Rx sectors, respectively.	20 cm 20 cm
θ_T θ_R	Half power beamwidths of the Tx and Rx antennas in the x-y plane (relative to x-axis), respectively.	[-7.5º , 7.5º] [-7.5º , 7.5º]
v_{TS} v_{RS}	The relative velocities of the moving scatterers with respect to velocities of the Tx and Rx, respectively.	5.61 cm/s 5.61 cm/s
$f_{TS\,\max}$ $f_{RS\,\max}$	The maximum Doppler frequencies associated with the moving scatterers around the Tx and Rx, respectively.	56.1 Hz 56.1 Hz
$\alpha_{TM}^{(k)}$ $\alpha_{RM}^{(l)}$	The angle of departure (AoD) and the angle of arrival (AoA) from moving scatterers, respectively.	[-7.5º , 7.5º] [-7.5º , 7.5º]
$\gamma_{TS}^{(k)}$ $\gamma_{RS}^{(l)}$	The directions of moving scatterers around the Tx and Rx, respectively, in the x-y plane (relative to the x-axis).	[0 , 2π) [0 , 2π)
ε_{pk} , ε_{kq} , ε_{pl} , ε_{lq}	The distances $A_T^{(p)}$–$S_{TM}^{(k)}$, $S_{TM}^{(k)}$–$A_R^{(q)}$, $A_T^{(p)}$–$S_{RM}^{(l)}$, $S_{RM}^{(l)}$–$A_R^{(q)}$	$\varepsilon_{pk} = \varepsilon_{lq}$ = 20 cm $\varepsilon_{pl} = \varepsilon_{kq}$ = 20 cm
λ	The wavelength.	1 mm
K	The Rice factor.	5
u k	The von Mises pdf parameters: 1) u, mean angle where the scatterers are distributed in the x-y plane; 2) k, spread of scatterers around the mean.	0 0.3
η_{TM} η_{RM}	Specify how much the scattered rays from moving scatterers around the Tx and Rx contribute in the total averaged power.	0.5 0.5

To verify the geometrical model with measurements, we need to estimate the model parameters from the measured data. The relative velocities of the moving scatterers, i.e., cables, and the maximum Doppler frequencies are estimated from the spectrogram in Fig. 7, where a maximum Doppler frequency is observed as 56.1 Hz, corresponding to $v_{TS} = v_{RS} =$ 5.61 cm/s. Note that the images on both sides of the carrier signal at 300 GHz are caused by sub-carrier artifacts (due to nonlinearity in the system). A zoom-in view in Fig. 7 shows that the Doppler effect on the artifact sub-carriers did not cause the inter-carrier interference. The parameters in the von Mises PDF and the Rice parameter K are estimated from the measured input delay-spread functions, where $(\mu, \kappa) =$ (0, 0.3) and $K = 5$, respectively. We assume $\eta_{TM} = \eta_{RM} = 0.5$. Detailed values of the parameters used in the proposed model are summarized in the third column in Table II.

Figure 8 presents the modeled autocorrelation function, and Fig. 9 presents the measured and modeled DPS, respectively. We can observe that both the modeled and measured DPS are similar to the "bell-shape" spectra in [12]–[15], where both the transmitter and the receiver are stationary, and time-variations are due to the movement of the scatterers. We have

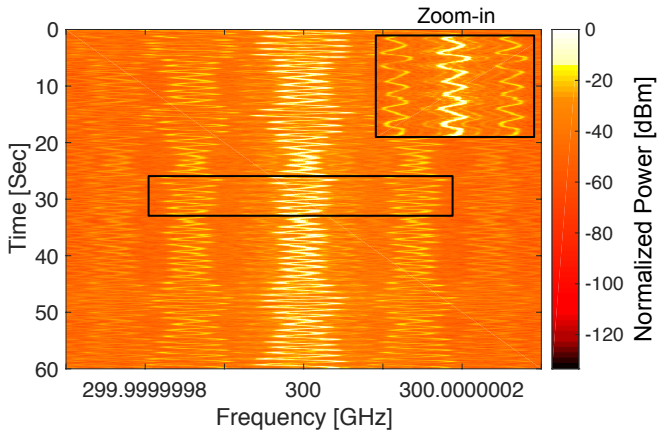

Fig. 7. Spectrogram of the measured narrow-band channel impulse response at 300 GHz.

also observed that the modeled DPS has a good agreement with measured data.

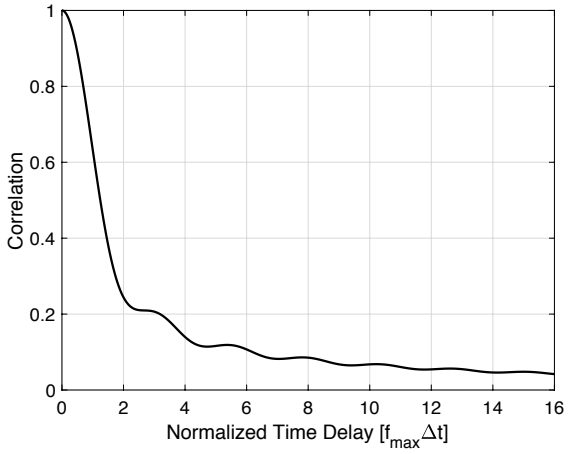

Fig. 8. Modeled autocorrelation function.

IV. Conclusions

A THz channel measurement campaign in a data center environment and its corresponding results have been presented. The statistics of amplitude fading in a 4×4 MIMO channel have been investigated with results showing an m-Nakagami distribution fit and a linear dependency on delay bins. Furthermore, Doppler shift in THz bands due to the effect of cooling airflow turbulence, which causes cables to vibrate has also been measured. A 2-D geometrical propagation model that includes moving scatterers is introduced. From the 2-D model, the corresponding DPS is derived and validated with measured data. Results show that a maximum Doppler frequency is observed as 56.1 Hz.

References

[1] S. Mollahasani and E. Onur, "Evaluation of Terahertz Channel in Data Centers," in *NOMS 2016 - 2016 IEEE/IFIP Network Operations and Management Symposium*, Apr. 2016, pp. 727–730.

[2] A. Davy, L. Pessoa, C. Renaud, E. Wasige, M. Naftaly, T. Kürner, G. George, O. Cojocari, N. O. Mahony, and M. A. G. Porcel, "Building An End User Focused THz Based Ultra High Bandwidth Wireless Access Network: the TERAPOD Approach," in *9th International Congress on Ultra Modern Telecommunications and Control Systems and Workshops (ICUMT)*, Nov. 2017, pp. 454–459.

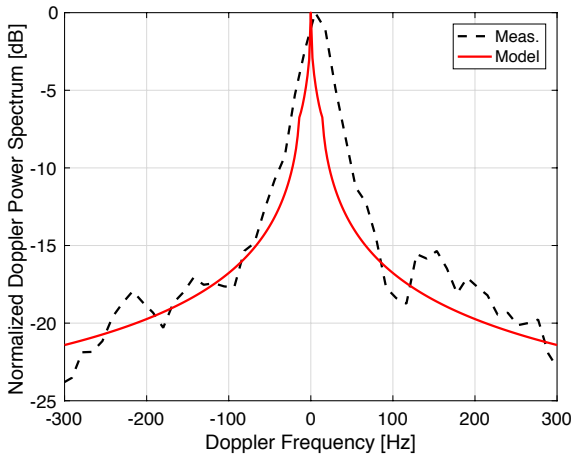

Fig. 9. Measured and modeled Doppler power spectra (DPS).

[3] V. Petrov, J. Kokkoniemi, D. Moltchanov, J. J. Lehtomäki, Y. Koucheryavy, and M. J. Juntti, "Last Meter Indoor Terahertz Wireless Access: Performance Insights and Implementation Roadmap," *IEEE Communications Magazine*, vol. 56, no. 6, pp. 158–165, Jun. 2018.

[4] B. Peng and T. Kürner, "A Stochastic Channel Model for Future Wireless THz Data Centers," in *International Symposium on Wireless Communication Systems (ISWCS)*, Aug. 2015, pp. 741–745.

[5] N. Boujnah, S. Ghafoor, and A. Davy, "Modeling and Link Quality Assessment of THz Network Within Data Center," in *2019 European Conference on Networks and Communications (EuCNC)*, Jun. 2019, pp. 57–62.

[6] J. M. Eckhardt, T. Doeker, S. Rey, and T. Kürner, "Measurements in a Real Data Centre at 300 GHz and Recent Results," in *2019 13th European Conference on Antennas and Propagation (EuCAP)*, Mar. 2019, pp. 1–5.

[7] C.-L. Cheng and A. Zajić, "Characterization of 300 GHz Wireless Channels for Rack-to-Rack Communications in Data Centers," in *2018 IEEE 29th Annual International Symposium on Personal, Indoor, and Mobile Radio Communications (PIMRC)*, Sep. 2018.

[8] C.-L. Cheng, S. Sangodoyin, and A. Zajić, "THz MIMO Channel Characterization for Wireless Data Center-Like Environment," in *2019 IEEE International Symposium on Antennas and Propagation USNC/URSI National Radio Science Meeting*, Jul. 2019.

[9] C.-L. Cheng and A. Zajić, "Characterization of Propagation Phenomena Relevant for 300 GHz Wireless Data Center Links," *IEEE Transactions on Antennas and Propagation*, (under revision).

[10] *Custom Transmitters*, Virginia Diodes, Inc., Charlottesville, VA, USA. [Online]. Available: http://vadiodes.com/en/products/custom-transmitters

[11] Gigazine. (2008) Compare Cables That Are Tangled Together and Cables Organized Beautifully Like Art. [Online]. Available: https://gigazine.net/gsc_news/en/20081020_dirty_clean_cable/

[12] S. J. Howard and K. Pahlavan, "Doppler Spread Measurements of Indoor Radio Channel," *Electronics Letters*, vol. 26, no. 2, pp. 107–109, Jan. 1990.

[13] J. B. Andersen, J. O. Nielsen, G. F. Pedersen, G. Bauch, and G. Dietl, "Doppler Spectrum From Moving Scatterers in a Random Environment," *IEEE Transactions on Wireless Communications*, vol. 8, no. 6, pp. 3270–3277, Jun. 2009.

[14] S. Thoen, L. Van der Perre, and M. Engels, "Modeling the Channel Time-Variance for Fixed Wireless Communications," *IEEE Communications Letters*, vol. 6, no. 8, pp. 331–333, Aug. 2002.

[15] A. Zajić, "Impact of Moving Scatterers on Vehicle-to-Vehicle Narrow-Band Channel Characteristics," *IEEE Transactions on Vehicular Technology*, vol. 63, no. 7, pp. 3094–3106, Sep. 2014.

[16] A. Abdi, J. A. Barger, and M. Kaveh, "A Parametric Model for the Distribution of the Angle of Arrival and the Associated Correlation Function and Power Spectrum at the Mobile Station," *IEEE Transactions on Vehicular Technology*, vol. 51, no. 3, pp. 425–434, May 2002.